

# Nanoscale

Accepted Manuscript



This is an *Accepted Manuscript*, which has been through the Royal Society of Chemistry peer review process and has been accepted for publication.

*Accepted Manuscripts* are published online shortly after acceptance, before technical editing, formatting and proof reading. Using this free service, authors can make their results available to the community, in citable form, before we publish the edited article. We will replace this *Accepted Manuscript* with the edited and formatted *Advance Article* as soon as it is available.

You can find more information about *Accepted Manuscripts* in the [Information for Authors](#).

Please note that technical editing may introduce minor changes to the text and/or graphics, which may alter content. The journal's standard [Terms & Conditions](#) and the [Ethical guidelines](#) still apply. In no event shall the Royal Society of Chemistry be held responsible for any errors or omissions in this *Accepted Manuscript* or any consequences arising from the use of any information it contains.

# Microscopic mechanisms of vertical graphene and carbon nanotube cap nucleation from hydrocarbon growth precursors

Umedjon Khalilov, Annemie Bogaerts, and Erik C. Neyts

Department of Chemistry, Research Group PLASMANT, University of Antwerp, Universiteitsplein 1, 2610 Wilrijk, Antwerp, Belgium

## Abstract

Controlling and steering the growth of single walled carbon nanotubes is often believed to require controlling the nucleation stage. Yet, little is known about the microscopic mechanisms governing the nucleation from hydrocarbon molecules. Specifically, we address here the dehydrogenation of hydrocarbon molecules and the formation of all-carbon graphitic islands on metallic nanoclusters from hydrocarbon molecules under conditions typical for carbon nanotube growth. Employing reactive molecular dynamics simulations, we demonstrate for the first time that the formation of a graphitic network occurs through the intermediate formation of vertically oriented, not fully dehydrogenated graphitic islands. Upon dehydrogenation of these vertical graphenes, the islands curve over the surface, thereby forming a carbon network covering the nanoparticle. The results indicate that controlling the extent of the dehydrogenation offers an additional parameter to control the nucleation of carbon nanotubes.

## Introduction

Carbon nanotubes in general and single walled carbon nanotubes in particular continue to attract widespread attention, thanks to their unique properties.<sup>1</sup> Especially the fact that the electronic properties can be tuned by changing fundamental CNT properties such as the diameter

and chirality drives continued research on growth control, both experimentally and computationally.

The most often used experimental growth technique for CNTs is chemical vapor deposition, in which a hydrocarbon gas is catalytically dissociated at the surface of a suitable nanocatalyst particle at elevated temperature.<sup>2</sup> The elevated temperature in combination with the Gibbs-Thomson effect,<sup>3,4</sup> however, prevents the catalyst surface from maintaining a crystalline structure, thus making epitaxial growth impossible. Growth at lower temperature might be possible using plasma enhanced CVD, where the gas is activated in the plasma phase instead of on the catalyst surface.<sup>5-8</sup> If the growth temperature can be sufficiently lowered, epitaxial growth might be possible. The main obstacle at low temperature, however, is the cap formation and lift-off during the nucleation stage.<sup>9</sup>

In spite of the large number of papers dealing with this topic, the nucleation and growth of CNTs is still not fully understood. This is in part due to the difficulty to access the incubation and nucleation stage directly in the experiment. Complementary to experimental studies, atomic scale simulations are thus very useful to gain insight in the microscopic processes taking place. As a result, carbon nanotube growth has often been simulated, studying a variety of effects, including the (non) requirement of a temperature gradient,<sup>10,11</sup> the catalyst particle size,<sup>12,13</sup> the effect of applying an electric field,<sup>14</sup> the influence of ion bombardment,<sup>15,16</sup> the interaction strength between metal and carbon network,<sup>9,17</sup> the effect of the support-nanoparticle interaction strength,<sup>18,19</sup> the necessity of a carbide phase, both for Ni and Fe,<sup>20-23</sup> the effect of the carbon chemical potential,<sup>24,25</sup> and the importance of metal-mediated defect healing.<sup>26,27</sup> Recent reviews on modeling CNT growth can be found in references.<sup>7, 28, 29</sup>

One important assumption made in all of these simulations, however, is the use of pure carbon as the sole growth precursor, thus assuming instantaneous hydrocarbon decomposition on the catalyst surface. Hydrogen is thus never considered in any of these simulations. Balbuena et al. recently studied the influence of the growth precursor, using either C atoms or C<sub>2</sub> dimers as input gas.<sup>30</sup> These authors found that the C<sub>2</sub> precursor dissolves more slowly in the metal nanoparticle, and leads to less carbon association within the particle. Surface diffusion and nucleation from C<sub>2</sub> were found to be accelerated, increasing the risk of nanoparticle encapsulation. Also Shariat et al. employed two growth species, viz. thermalised C-atoms and

energetic C-ions (modeled as fast neutrals), to mimic PECVD growth at low temperature.<sup>16</sup> These authors found that at 500 K, CNT-growth is promoted when the ion energy is in the order of 60 eV.

Shibuta et al. very recently performed ab initio molecular dynamics simulations to study the decomposition of methane on a Ni(111) surface for graphene growth,<sup>31</sup> which is closely related to CNT growth.<sup>28</sup> These simulations demonstrated that CH<sub>4</sub> is stepwise decomposed into C and 4H, in agreement with classical MD simulations by Somers et al.<sup>32</sup> and Liu et al.<sup>33</sup> In this decomposition process, both CH<sub>3</sub> and CH are found as stable chemisorbed species on the nickel surface. The C atoms then diffuse into the subsurface region while the H atoms diffuse over the surface. Note, however, that in all of these simulations, the Ni surface was perfectly crystalline, without the curvature normally associated with nanocatalyst particles used for CNT growth.

Until now, there are no reports on the atomistic mechanisms during nucleation of a cap or the growth of a CNT from a hydrocarbon source gas. In this work, we present the simulated formation of a graphitic network on Ni-nanocatalyst particles from acetylene (C<sub>2</sub>H<sub>2</sub>) and benzene (C<sub>6</sub>H<sub>6</sub>), two hydrocarbon gases which are known experimentally to yield CNTs.<sup>34</sup>

## Computational details

Our simulations are based on combined molecular dynamics (MD) and time-stamped force-bias Monte Carlo (tfMC) simulations,<sup>35</sup> which were previously demonstrated to yield CNTs with definable chiralities.<sup>27,36</sup> In these simulations, energies and forces are derived from the ReaxFF interatomic potential,<sup>37</sup> using parameters developed by Mueller et al.<sup>38</sup> Previously, we demonstrated that this force field faithfully reproduces various key properties of the Ni/C system, relevant for Ni-based CNT growth, including the C-C clustering energy, the C heat of solution in Ni and the formation volume of a C interstitial in bulk Ni.<sup>27</sup> This force field also produces binding energies of hydrogen and a wide variety of hydrocarbons on nickel in close agreement with quantum chemical calculations.<sup>38</sup> Moreover, of particular importance for the current work is the excellent agreement found between this force field and quantum chemical calculations found for dehydrogenation barriers on nickel.<sup>38</sup>

In our simulations, growth is accomplished by allowing hydrocarbon molecules (C<sub>2</sub>H<sub>2</sub> or C<sub>6</sub>H<sub>6</sub>) to impinge on a Ni<sub>55</sub> nanocluster. At any moment in time, the total number of gas phase

molecules is kept constant. Thus, when a molecule impinges on and sticks to the nanocluster a new molecule is introduced in the simulation box. When a hydrocarbon molecule adsorbs on the Ni cluster, the resulting structure is allowed to relax by application of tfMC.<sup>35</sup> During this relaxation stage, no new molecules are allowed to impinge on the cluster.

The pressure of the system is related to the impingement rate that we target in our simulations. In the ideal gas approximation, the impingement flux can be calculated as:

$$J\left(\frac{\text{molecules}}{\text{m}^2}\cdot\text{s}\right) = \frac{N_A p}{\sqrt{2\pi MRT}}$$

where  $N_A$  is Avogadro's number,  $p$  is the pressure (in Pa),  $M$  is the molar mass (in kg/mole),  $R$  is the universal gas constant and  $T$  is the temperature (in K). The impingement fluxes simulated in this work are  $0.02 \text{ nm}^{-2}\cdot\text{ns}^{-1}$ ,  $0.1 \text{ nm}^{-2}\cdot\text{ns}^{-1}$ ,  $0.2 \text{ nm}^{-2}\cdot\text{ns}^{-1}$ ,  $1.0 \text{ nm}^{-2}\cdot\text{ns}^{-1}$  and  $2.0 \text{ nm}^{-2}\cdot\text{ns}^{-1}$ , corresponding to a minimal pressure of 1.46 kPa (for acetylene at 1600 K and an impingement flux of  $0.02 \text{ nm}^{-2}\cdot\text{ns}^{-1}$ ), and a maximal pressure of 270 kPa (for benzene at 1600 K and an impingement flux of  $2 \text{ nm}^{-2}\cdot\text{ns}^{-1}$ ). For the highest impingement flux ( $2 \text{ molecules}\cdot\text{nm}^{-2}\cdot\text{ns}^{-1}$ ), simulations were also carried out at 1000 K and 1400 K. For all other fluxes, the temperature was set to 1600 K, controlled by the canonical Bussi thermostat.<sup>39</sup> The average time between two impacts varies between 0.5 ns (for the highest impingement flux) and 50 ns (for the lowest impingement flux). The maximum total simulation time realized in these simulations was 2  $\mu\text{s}$ .

The Ni cluster is either a gas phase cluster, or a surface-bound cluster. In the case of a surface-bound cluster, the cluster is physisorbed on a virtual surface. This physisorption interaction is expressed by a one-dimensional averaged Lennard-Jones potential:<sup>40</sup>

$$F(z) = D_e \left\{ \frac{1}{5} \left( \frac{\sigma}{z} \right)^{10} - \frac{1}{2} \left( \frac{\sigma}{z} \right)^4 \right\},$$

where  $z$  is the atomic coordinate normal to the substrate. By choosing the  $D_e$  and  $\sigma$  parameters, a specific substrate can be mimicked. To study the influence of this substrate, we have chosen aluminum, which the parameters are  $D_e = 2.3 \text{ eV}$  and  $0.03 \text{ eV}$ , and  $\sigma = 2.37 \text{ \AA}$  and  $2.976 \text{ \AA}$  for Ni-Al and C-Al pairs, respectively.<sup>41</sup>

For each distinct simulation condition (corresponding to a given combination of flux, temperature, and growth species, resulting in 36 different conditions), three to five independent simulations were carried out. The specific results described below correspond to a flux of 2 molecules.nm<sup>-2</sup>.ns<sup>-1</sup>, unless specifically stated otherwise.

## Results and discussion

### 1. Adsorption, desorption and pyrolysis

In Figure 1, the typical C<sub>2</sub>H<sub>2</sub> adsorption, dehydrogenation and subsequent H<sub>2</sub> desorption process at 1600 K is shown in a series of MD snapshots. The C<sub>2</sub>H<sub>2</sub> molecule travels through the simulation box until it impinges on the Ni-cluster.

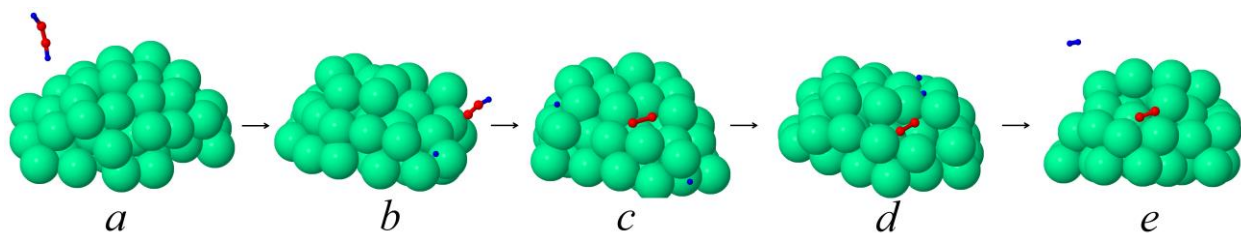


**Figure 1** Snapshots of structures observed during C<sub>2</sub>H<sub>2</sub> decomposition on a surface-bound Ni cluster: (a) a C<sub>2</sub>H<sub>2</sub> molecule moves randomly in vacuum before interacting with the Ni cluster; (b) the molecule loses one of its hydrogen atoms upon impact on the cluster; both the C<sub>2</sub>H radical and the H atom diffuse over the cluster surface; (c, d) dehydrogenation to a C<sub>2</sub> dimer; (e) finally, the hydrogen atoms recombine and desorb as a H<sub>2</sub> molecule; C<sub>2</sub> diffuses into the cluster and eventually the C-C bond may be broken.

Upon impingement, the molecule adsorbs dissociatively with the formation of an acetylide C<sub>2</sub>H radical and a H-atom. Also the second H-atom subsequently dissociates from the acetylide radical. The remaining C<sub>2</sub> dimer is found to diffuse back and forth into the first subsurface layer of the Ni cluster. Indeed, it was previously found from tight-binding simulations that C<sub>2</sub> dimers are stable in the Ni-subsurface region.<sup>42</sup> The H-atoms diffuse over the surface of the cluster, until they recombine and desorb as H<sub>2</sub>. Employing nudged elastic band calculations,<sup>43</sup> we calculated the activation barrier for H-diffusion as E<sub>a</sub>=0.63 eV, while the recombination

activation energy is found to be  $E_a=1.63$  eV.<sup>32</sup> H atoms may thus freely diffuse over the Ni surface until they either collide and recombine with another H atom and desorb as  $H_2$ .

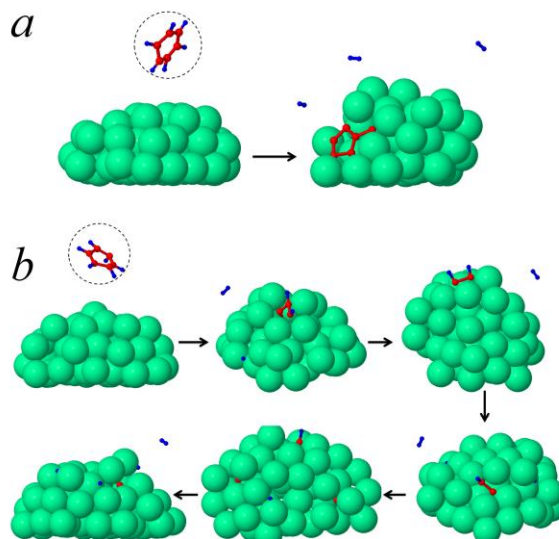


**Figure 2** - Dehydrogenation processes for benzene: (a) complete dehydrogenation upon impact, with reorganization of the benzene ring in a pentagon; (b) gradual dehydrogenation and C-C bond cleavage, leading to dissolution of carbon in the cluster.

In spite of the higher molecular adsorption rate of acetylene, the dehydrogenation mechanism is similar for  $C_2H_2$  and  $C_6H_6$ . We found that upon adsorption,  $C_6H_6$  either loses all of its hydrogen atoms more or less simultaneously, leaving the carbon atoms connected as a hexagon or reconstructing them to a pentagon, or alternatively, all of its C-H as well as C-C bonds are gradually broken and its C atoms eventually dissolve into the cluster. Both mechanisms are illustrated in Figure 2. Especially at a high impingement flux, the adsorbed benzene molecules do not dehydrogenate completely but rather form stable  $C_6H_4$  or  $C_6H_3$  rings standing vertically on the cluster surface. This is in agreement with simulations by Mueller who found that  $C_6H_3$  converts to  $C_5H_3$  and further decomposes by breaking either C-C or C-H bonds starting from a temperature  $T=1750$  K.<sup>44</sup> A more detailed description of the dehydrogenation and graphitic network formation process will be presented below.

Hydrogen atoms at the surface of the cluster may bind with a previously adsorbed and partially dehydrogenated hydrocarbon molecule, such as the  $C_2H$  (in  $C_2H_2$  case) or  $C_6H_3$  (in  $C_6H_6$  case) radicals, as well as larger radicals, and then rehydrogenate the hydrocarbon.

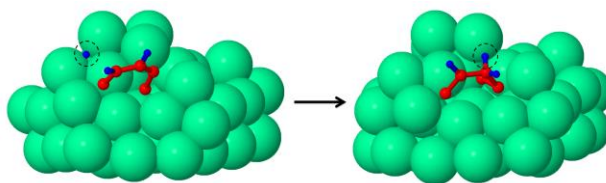


**Figure 3** – Rehydrogenation of a previously adsorbed  $C_5H_2$  hydrocarbon chain, slowing down the overall dehydrogenation rate. The H atom that is attached again to the  $C_5H_2$  chain is indicated with a black dashed circle.

An example of a rehydrogenation event is illustrated in Figure 3 for a surface-bound  $C_5H_2$  hydrocarbon chain during acetylene adsorption. Note that the appearance of such free-standing hydrocarbon chains may lead to the formation of carbon nanosheets.<sup>45</sup>

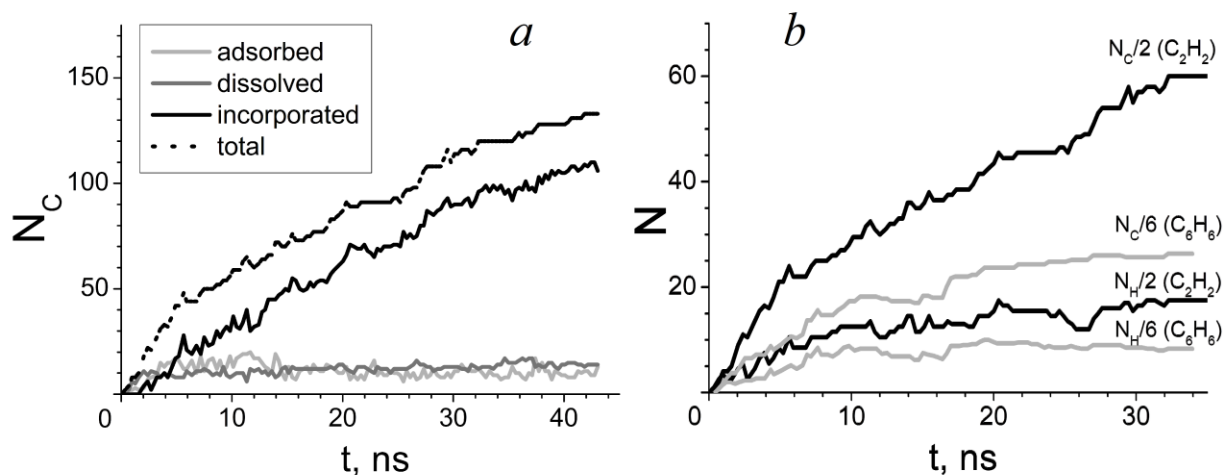


**Figure 4** – (a) Evolution of the number of adsorbed, dissolved, incorporated and total carbon atoms in the case of acetylene impact; (b) Evolution of the total number of carbon ( $N_C$ ) and hydrogen ( $N_H$ ) atoms in/on the Ni cluster during the nucleation process, upon impact of either acetylene or benzene molecules. The number of adsorbed C or H atoms upon  $C_2H_2$  and  $C_6H_6$  impact is divided by two and six, respectively, to allow a better comparison.

Impinging gas phase hydrocarbon species adsorb on the surface of the Ni cluster, as explained in the previous paragraphs, and subsequently dissociate and dissolve into the cluster



where they preferentially occupy subsurface sites. Thus, at the beginning of the nucleation process, the number of adsorbed and dissolved carbon atoms rapidly rises as shown in Figure 4a. The time shown corresponds to the sum of all MD+tfMC cycles.<sup>35</sup> Note that surface-adsorbed C atoms still have bonds to H atoms, and must first lose all their hydrogen atoms in order to dissolve into the cluster. Subsequently, carbon atoms move into the bulk of the cluster, and then either quickly return to the surface or remain in the subsurface region. This process continues until there is no room left for additional carbon atoms to be added without forming C-C bonds at the surface or occasionally in the subsurface region. In the figure, therefore, the number of dissolved atoms remains constant (about 10) after saturation. The number of carbon atoms incorporated in the carbon network increases following the same trend as the total number of C atoms. The graph is similar for the C<sub>6</sub>H<sub>6</sub> case.

In Figure 4b, the evolution of the number of C-atoms and H-atoms in the structure is also shown as a function of simulation time for growth from C<sub>2</sub>H<sub>2</sub> and growth from C<sub>6</sub>H<sub>6</sub>. The number of all C-atoms, i.e., excluding vacuum atoms, is seen to continuously increase, both in the case of C<sub>2</sub>H<sub>2</sub> and C<sub>6</sub>H<sub>6</sub>. Note that  $N_C/2$  and  $N_C/6$  are plotted for acetylene and benzene, respectively, to correlate with the number of incorporated/adsorbed/dissolved carbon atoms. It is clear that after the first 6 ns, the number of all C atoms is three times as high for acetylene compared to benzene, so the adsorption rate of C<sub>2</sub>H<sub>2</sub> is about three times higher than that of C<sub>6</sub>H<sub>6</sub>. However, the total number is nearly identical in both cases, as acetylene contains 2 and benzene contains 6 C-atoms. From this figure, it is also clear that the H-concentration stagnates to some constant value, and thus the net H-incorporation goes to zero after the initial start of the growth process, because of the desorption as H<sub>2</sub>.

H<sub>2</sub> desorption from the cluster surface is essential for enabling the formation of a graphene network on the surface of the catalyst. It is found that hydrogen desorption (as H<sub>2</sub>) does not require a critical minimum surface concentration of hydrogen atoms. Instead, H<sub>2</sub> desorption is found to occur as soon as the first hydrocarbon molecules adsorb on the surface, as shown in Figure 5. Furthermore, it is clear from this figure that the H<sub>2</sub> desorption rate upon benzene and acetylene impact is similar, keeping in mind that benzene has three times more H atoms than acetylene.

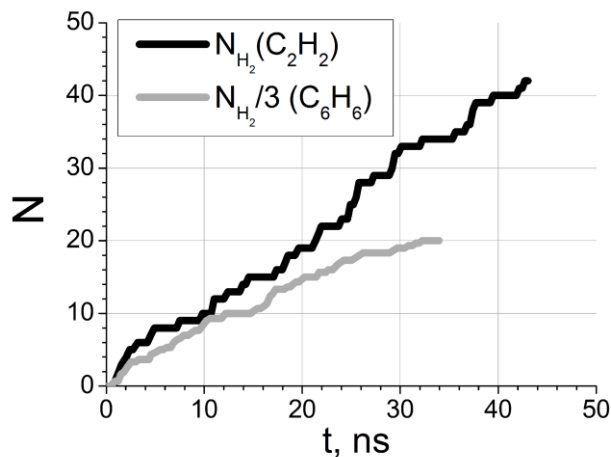


**Figure 5** – Evolution of the number of desorbed  $H_2$  molecules during the adsorption of either  $C_2H_2$  or  $C_6H_6$  molecules. Note that the number of desorbed  $H_2$  molecules upon  $C_6H_6$  impact is divided by three, to allow a better comparison with  $C_2H_2$  impact.

It is known that hydrogen helps in the activation of the catalyst particles as well as enhances the yield of the growth. Furthermore, hydrogen diminishes the decomposition of the hydrocarbon feedstock and prevents excess carbon deposition at the surface of the catalyst particles. On the other hand, it may also hinder the formation of graphite-like carbon,<sup>46,47</sup> if its concentration is too high. Zhang et al.<sup>47,48</sup> and Behr et al.<sup>49</sup> also suggested that a plasma including H atoms causes the breaking up of the  $sp^2$  C-C bonds and the formation of  $sp^3$  C-H bonds, resulting in etching of the carbon nanotubes.

Both  $C_6H_6$  and  $C_2H_2$  molecules are also found to dissociate in the gas phase at 1600 K, such that in this case also the decomposition products may impinge on and bind with the nickel cluster. This gas phase pyrolysis is in agreement with experimental studies showing the formation of acetylene, ethylene, methane, carbon, as well as a variety of other species.<sup>50-58</sup> Thus, the gas phase also contains a fraction of  $C_xH_{x-y}$  species. Under high flux and high temperature conditions, we find that up to 50% of the benzene molecules are transformed into other species, most notably acetylene molecules.<sup>57</sup> In the case of acetylene, gas phase pyrolysis occurs for about 40% of the molecules. In this case, mostly  $C_2$  dimers and acetylide  $C_2H$  radicals are found as pyrolysis products.<sup>47,48</sup> A detailed analysis of the pyrolysis mechanisms for both  $C_6H_6$  and  $C_2H_2$  is presented in Tables 1 and Table 2 as supplementary data. Note that in contrast to the

experiments, polyaromatic rings are not formed in our simulations, as the pyrolysis products rapidly adsorb on the nickel cluster. Additionally, we find that at high temperature, molecules often lose a H-atom upon impingement, and the resulting  $C_xH_{x-1}$  radical is scattered from the surface into the gas phase. The H-atom may remain on the surface or also scatter into the gas phase. The resulting gas phase H-atoms may also recombine with the gas phase hydrocarbon radicals. Our calculations show also that the appearance of these gas phase decomposition products depends only slightly on the pressure. As we here focus on the formation of a graphitic network from either  $C_2H_2$  or  $C_6H_6$ , we limit the influence of the gas phase pyrolysis products and hydrogen gas<sup>46</sup> and remove these products every  $10^6$  simulation steps.

## 2. $k$ -coefficient

As mentioned above, the crucial role of the catalytic hydrocarbon decomposition in catalyzed carbon nanotube growth will determine the adsorption/desorption rate of H atoms and whether or not tube growth may occur.<sup>46-49</sup> In other words, incorporation of carbon atoms in the carbon network on the catalyst is enhanced when hydrogen extensively desorbs from the surface. We thus introduce a coefficient  $k$  in order to assess the dehydrogenation degree of the source gas on the catalytic metal cluster as follows:

$$k = \frac{mN_C - nN_H}{mN_C + nN_H}$$

where  $N_C$  and  $N_H$  are the number of carbon and hydrogen atoms respectively in the cluster,  $n$  and  $m$  are the number of carbon atoms and hydrogen atoms, respectively, in the impinging  $C_nH_m$  molecule/radical. The  $k$ -coefficient allows to easily differentiate between physisorption of the hydrocarbon on the cluster surface without any subsequent hydrogen desorption ( $k=0$ ), complete dehydrogenation and subsequent desorption of  $H_2$  ( $k=1$ ), and partial dehydrogenation and  $H_2$ -desorption ( $0 < k < 1$ ).

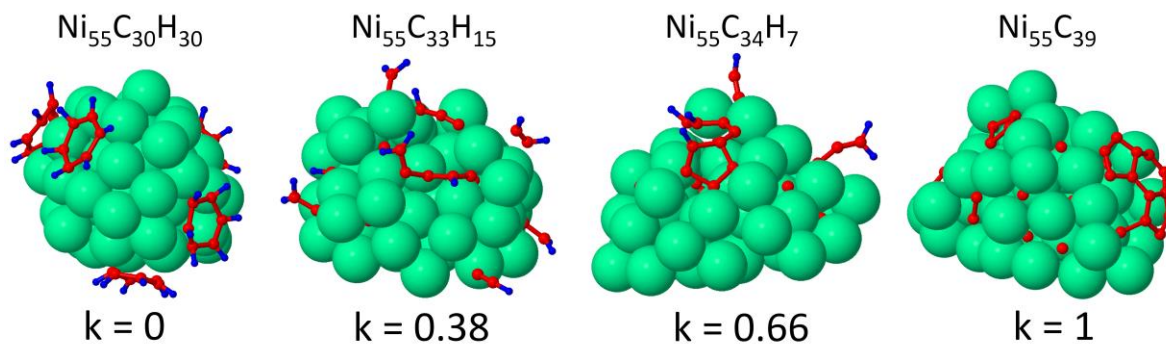


**Figure 6** –  $\text{Ni}_{55}\text{C}_y\text{H}_z$  structures corresponding to various  $k$ -coefficients, showing a gradually lower H-concentration for increasing  $k$  value.

In Figure 6, a series of Ni/C structures is shown for various values of the  $k$ -coefficient. An increasing value for  $k$  indicates a lower H-concentration at the surface, and thus a higher probability for carbon cluster coalescence and eventually cap formation. Thus,  $k=1$  (i.e.,  $N_H=0$ ) is the ideal surface condition for nanotube growth. Note that this condition corresponds to all nanotube growth simulations reported in literature so far.

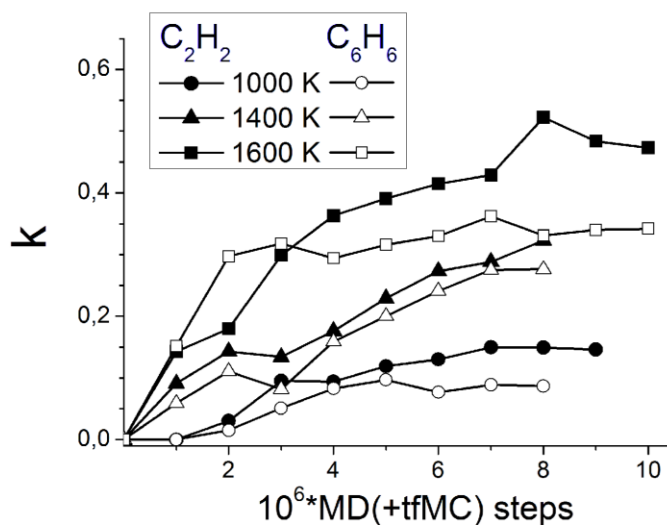


**Figure 7** – Evolution of the  $k$ -coefficient during either  $\text{C}_2\text{H}_2$  or  $\text{C}_6\text{H}_6$  adsorption, for three different cluster temperatures, for a surface-bound Ni-cluster.

The  $k$ -coefficient depends on the growth temperature and the type of carbon precursor.

A comparison between acetylene and benzene at various temperatures is shown in Figure 7, in terms of the  $k$ -coefficient as a function of the number of simulation steps. It can be seen that the  $k$ -coefficient, and thus the dehydrogenation efficiency, is somewhat higher for acetylene than for benzene at all temperatures investigated, as mentioned in previous section. Furthermore, the dehydrogenation increases with temperature, which is attributed to an increasing probability of H-recombination at the surface. Indeed, the latter has a high activation barrier of 1.63 eV as mentioned above. In general, the H<sub>2</sub> desorption and thus the  $k$ -coefficient will also depend on the hydrocarbon flux (or feedstock pressure), the cluster size and type of substrate which, however, we have not investigated here.

Also, we rely on the fact that the change in  $k$  is not directly indicative of how the decomposition has taken place, either by pyrolysis or catalysis. In the pyrolysis process, the precursor can lose some of its hydrogen atoms before it impinges on the catalyst particle. Hydrogen atoms in the gas phase, however, may in turn initiate another pyrolysis reaction or alternatively impinge on the catalyst surface. Consequently, both the decomposed molecule/radical and hydrogen atom eventually impinge on the cluster. In our simulations, all decomposed particles eventually chemisorb on the cluster. The hydrogen concentration at the surface (and thus the  $k$ -coefficient), is then determined by the subsequent desorption of H<sub>2</sub> molecules from the surface as well as the arrival rate of H atoms to the surface. Therefore, the  $k$ -coefficient does not depend on how the precursor decomposes.

### 3. Evolution of the cap nucleation process

The typical evolution of the carbon network on the Ni-cluster is shown in Figure 8, both for acetylene and benzene impact.

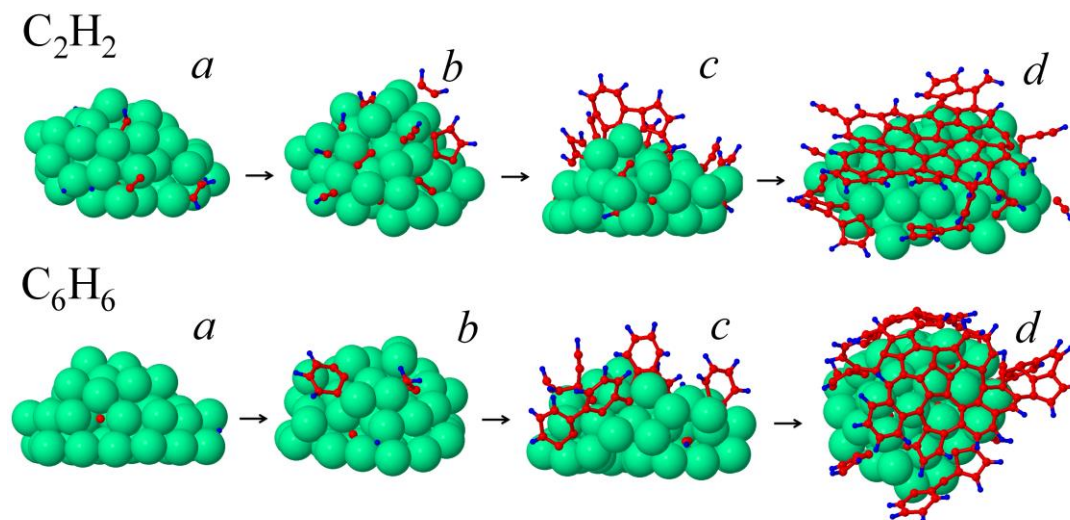


**Figure 8** – Evolution of the graphitic network formation process upon impact of acetylene and benzene: (a) in the initial stage, almost all adsorbed C atoms diffuse into the Ni cluster; (b) after saturation, initial rings are formed on the cluster; (c) subsequently, hydrogenated graphitic patches arrange in a vertical orientation; (d) after dehydrogenation, the graphene-like sheets curve over the surface and connect to form an extensive graphitic network, forming either a CNT cap or leading to encapsulation of the cluster.

The molecules initially adsorb after impingement, after which one or several C-H bonds are typically broken as described above, resulting in chemisorption (Figure 8a). The remaining radicals, however, are still very mobile, and can easily diffuse over the surface of the cluster. When C-atoms and C-dimers are formed through dehydrogenation and C-C bond cleavage, they can dissolve in and diffuse through the subsurface area of the cluster. Above the supersaturation limit, carbon also starts to segregate at the surface from the subsurface region, in accordance to the vapor-liquid-solid mechanism. In this stage, rings are easily formed on the surface (Figure 8b). As these rings are also mobile on the surface, they may concatenate, and form small graphitic islands. In contrast to growth from H-free precursors, however, these small islands, typically containing three or four rings, are not lying flat on the surface, but are standing upright, normal to the surface (Figure 8c). Such growth behavior is similar to the formation of carbon nanosheets in the initial stage of nanowall growth.<sup>45</sup> However, these patches gradually lose their hydrogen atoms and curve over the surface to connect to each other (Figure 8d). This

transformation from vertically oriented patches to horizontally oriented patches is displayed in more detail in Figure 9.

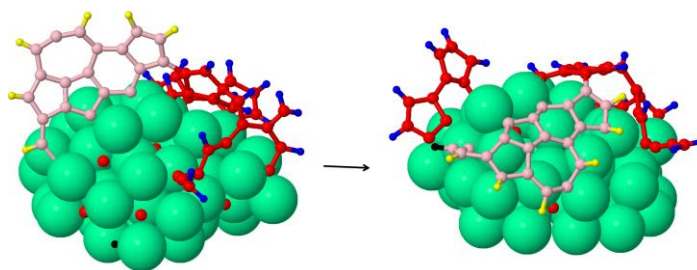


**Figure 9** – Dehydrogenation of the vertically oriented graphene sheets, leading to the formation of horizontally oriented graphene patches curving over the surface. The pink atoms denote the carbon patch that is transformed from standing upright to horizontally curved over the surface, while the red atoms denote all other carbon atoms.

Note that this transformation is required for cap nucleation to occur. Indeed, eventually, this concatenation process leads to the formation of either a graphitic cap or the encapsulation of the cluster. Also, we found both horizontal- and vertical-oriented patches in the same structure for both  $C_2H_2$  and  $C_6H_6$  impacts, in agreement with experiments reported by Malesevich et al.<sup>59</sup> They synthesized CNTs together with carbon nanowalls (CNWs) in one single experiment on a Ni coated substrate using an acetylene precursor. Furthermore, in a few cases, we observe that the addition of new hydrocarbon molecules to the structure occurs much faster than the dehydrogenation, leading to the formation of a number of parallel vertically oriented graphene sheets or CNWs as mentioned before. An example of this is shown in Figure 10. Note that these vertical sheets are almost defect-free, and consist of almost only hexagons. The distance between the sheets is about 3.0 Å, which is in fairly good agreement with experimental observations (3.4 Å).<sup>45,59</sup> Although we obtained such atomically thin, free-standing carbon nanosheets or CNWs as observed in many experimental works<sup>8</sup>, such nanosheets/nanowalls are experimentally mostly synthesized in a PECVD setup where electric fields are present. In contrast, our simulations were performed to mimic the CVD process and we thus assume that our vertical patches, which are not supported or stabilized by an electrical field, will eventually curve over the surface as the horizontal patches.

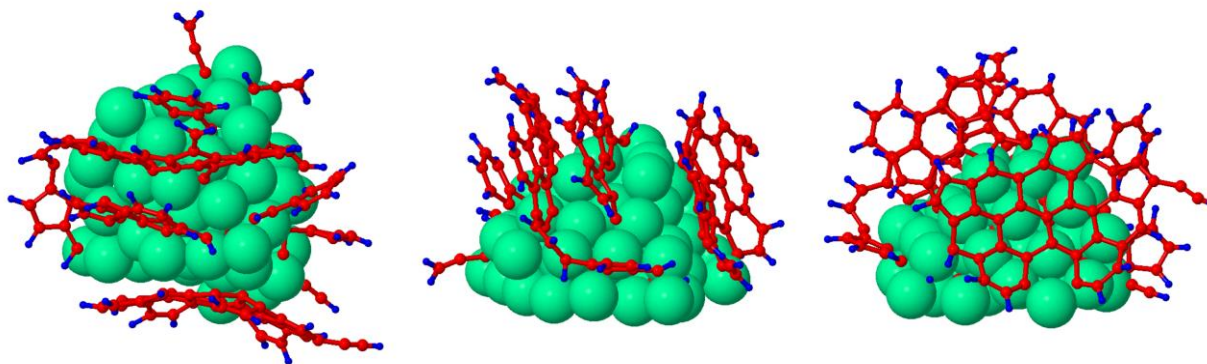


**Figure 10** – formation of vertically oriented graphene patches in top view (left), side view (middle) and front view (right). The figure shows that the patches are of high quality (i.e., consisting of almost exclusively hexagons), and the edges are fully hydrogenated.

In the cap nucleation process, we can distinguish three stages, as shown in Figure 11. In this figure, the evolution of the number of graphitic rings (counted as the sum of all pentagons, hexagons and heptagons) as well as the  $k$ -coefficient is shown as a function of time. It can be seen that the  $k$ -coefficient converges rapidly to a value around 0.4, with a slightly higher value for acetylene than for benzene impact. We denote the initial stage as the time in which the value for  $k$  rises, after which it continues to increase slowly. The number of graphitic rings is still negligible in this stage. In the second stage, vertically oriented graphitic islands (denoted by “vertical rings”) are formed, but no horizontal graphitic islands (denoted by “horizontal rings”), i.e., no graphitic patches curving over the surface are formed yet. As mentioned above, the vertically oriented graphitic patches gradually lose hydrogen atoms at their edges, either by recombination of H-atoms in the vertical patch, or by migration to the cluster and recombination on the cluster surface. This leads to a local increase in the  $k$ -coefficient, although the overall value of the  $k$ -coefficient stays more or less constant, and the patches start to curve over the surface. We denote the third stage when besides vertically oriented patches also horizontally oriented graphitic patches are formed. Specifically, the onset of the third stage is characterized by a transformation of vertically oriented patches to horizontally oriented patches.



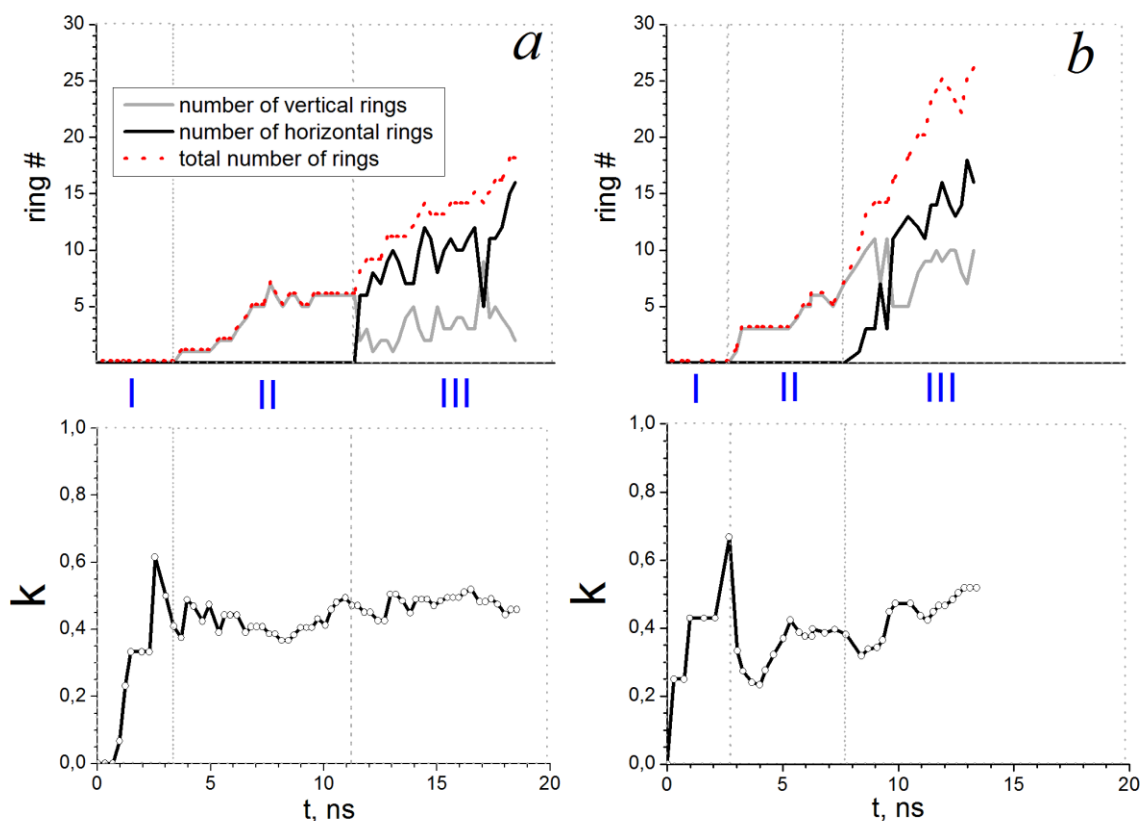


**Figure 11** – Upper panel: Number of rings (summed over pentagons, hexagons, and heptagons) as a function of time during the nucleation stage at an impingement flux of  $2 \text{ nm}^{-2} \cdot \text{ns}^{-1}$ , for acetylene (a) and benzene (b). The dotted red line is the total number of rings, the solid grey line is the number of vertical rings (i.e., rings in vertically oriented patches), and the solid black line is the number of horizontal rings (i.e., rings in patches curving over the surface). The three nucleation stages are denoted by roman numerals. The lower panel shows the evolution of the  $k$ -coefficient as a function of the simulated time.

From Figure 11, it is clear that benzene shows a higher tendency towards the formation of vertical patches, even in the third stage (as the ratio of vertical rings to horizontal rings is higher in the case of benzene), indicative of the more difficult dehydrogenation of benzene compared to acetylene, as discussed above. This also corresponds to the somewhat higher  $k$ -coefficients observed for acetylene as compared to benzene, as shown above in Figure 7b. Both in the case of acetylene and benzene, it is also clear that the number of vertically oriented rings (i.e., rings

pertaining to vertically oriented patches, normal to the surface) stagnates, while the number of rings parallel to the surface continues to increase. This is indeed a necessary condition for cap nucleation and lift-off. A cap-like structure, as formed in a growth simulation from benzene at 1600 K and at a pressure of 12.7 kPa is illustrated in Figure 12, both in top view and side view.

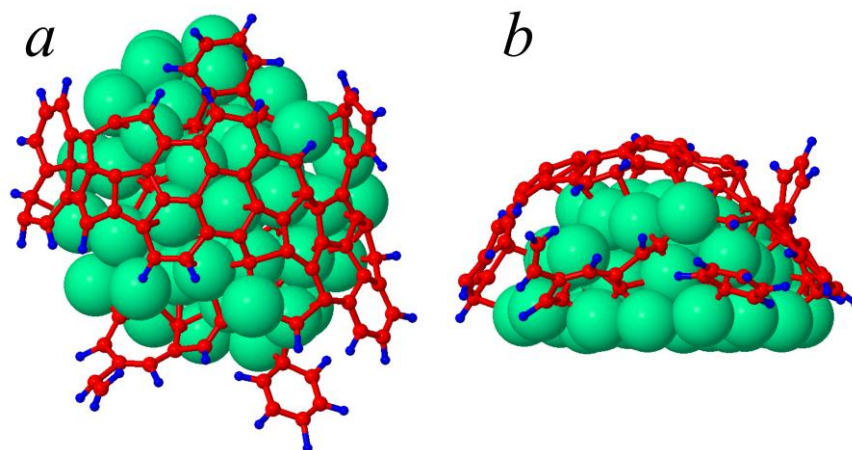


**Figure 12** – Cap-like structure formed from benzene impacts at 1600 K and 12.7 kPa in (a) top view, and (b) side view.

## Conclusions

Nucleation and growth of graphitic networks on Ni-nanoclusters from hydrocarbon molecules was studied employing reactive molecular dynamics simulations. While the vapor-liquid-solid mechanism is still found to be responsible for the segregation of carbon at the surface and the formation of some rings, we observe that graphitic islands on the catalyst are typically not fully dehydrogenated at their edges, leading to their vertical orientation. These vertical graphenes gradually lose their hydrogen atoms, allowing them to curve over the surface, connect, and form a continuous graphitic network. This leads to either cap formation or encapsulation of the nanocatalyst. These simulations provide a new insight in the nucleation of carbon nanotubes from hydrocarbon molecules.

## Acknowledgments

This work was carried out in part using the Turing HPC infrastructure at the CalcUA core facility of the Universiteit Antwerpen (UA), a division of the Flemish Supercomputer Center VSC, funded by the Hercules Foundation, the Flemish Government (department EWI) and the UA.

## References

- 1 M. Terrones, *Ann. Rev. Mater. Res.* 2003, **33**, 419-501.
- 2 W.-H. Chiang and R. M. Sankaran, *Nat. Mater.* 2009, **8**, 882-886.
- 3 Y. Shibuta and T. Suzuki, *Chem. Phys. Lett.* 2010, **498**, 323-327.
- 4 K. Ostrikov and H. Mehdipour *ACS Nano* 2011, **5**, 8372-8382.
- 5 E. J. Bae, Y. -S. Min, D. Kang, J.-H. Ko, W. Park, *Chem. Mater.* 2005, **17**, 5141-5145.
- 6 E. Mora, J. M. Pigos, F. Ding, B. I. Yakobson, A. R. Harutyunyan, *J. Am. Chem. Soc.* 2008, **130**, 11840-11841.
- 7 E. C. Neyts, *Vac. Sci. Technol. B* 2012, **30**, 030803.
- 8 K. Ostrikov, E. C. Neyts, M. Meyyappan, *Adv. Phys.* 2013, **62**, 113-224.
- 9 J. C. Burgos, H. Reyna, B. I. Yakobson, P. B. Balbuena, *Phys. Chem. C* 2010, **114**, 6952-6958.
- 10 F. Ding, A. Rosén, K. Bolton, *Chem. Phys. Lett.* 2004, **393**, 309-313.
- 11 F. Ding, A. Rosén, K. Bolton, *Carbon* 2005, **43**, 2215-2217.
- 12 Y. Shibuta, S. Maruyama, *Chem. Phys. Lett.* 2003, **382**, 381-386.
- 13 F. Ding, A. Rosén, K. Bolton, *Chem. Phys.* 2004, **121**, 2775-2779.
- 14 E. C. Neyts, A. C. T. van Duin, A. Bogaerts, *J. Am. Chem. Soc.* 2012, **134**, 1256-1260.
- 15 E. C. Neyts, K. Ostrikov, Z. J. Han, S. Kumar, A. C. T. van Duin, A. Bogaerts, *Phys. Rev. Lett.* 2013, **110**, 065501.
- 16 M. Shariat, S. I. Hosseini, B. Shokri, E. C. Neyts, *Carbon* 2013, **65**, 269-276.
- 17 M. A. Ribas, F. Ding, P. B. Balbuena, B. I. Yakobson, *J. Chem. Phys.* 2009, **131**, 224501.
- 18 D. A. Gomez-Gualdron, G. D. McKenzie, J. F. J. Alvarado, P. B. Balbuena, *ACS Nano* 2012, **6**, 720-735.
- 19 Y. Shibuta, J. A. Elliott, *Chem. Phys. Lett.* 2006, **427**, 365-370.
- 20 D. A. Gomez-Gualdron, P. B. Balbuena, *Carbon* 2013, **57**, 298-309.
- 21 Y. Ohta, Y. Okamoto, S. Irle, K. Morokuma, *ACS Nano* 2008, **2**, 1437-1444.

- 22 A. J. Page, H. Yamane, Y. Ohta, S. Irle, K. Morokuma, *J. Am. Chem. Soc.* 2010, **132**, 15699-15707.
- 23 A. Börjesson, K. Bolton, *J. Phys. Chem. C* 2010, **114**, 18045-18050.
- 24 H. Amara, J.-M. Roussel, C. Bichara, J.-P. Gaspard, F. Ducastelle, *Phys. Rev. B* 2009, **79**, 014109.
- 25 H. Amara, C. Bichara, F. Ducastelle, *Phys. Rev. Lett.* 2008, **100**, 056105.
- 26 M. Diarra, H. Amara, C. Bichara, F. Ducastelle, *Phys. Rev. B* 2012, **85**, 245446.
- 27 E. C. Neyts, A. C. T. van Duin, A. Bogaerts, *J. Am. Chem. Soc.* 2011, **133**, 17225-17231.
- 28 J. A. Elliott, Y. Shibuta, H. Amara, C. Bichara, E. C. Neyts, *Nanoscale* 2013, **5**, 6662-6676.
- 29 Y. Shibuta, *Diam. Relat. Mater.* 2011, **20**, 334-338.
- 30 D. A. Gomez-Gualdrón, J. M. Beetge, J. C. Burgos, P. B. Balbuena, *J. Phys. Chem. C* 2013, **117**, 10397-10409.
- 31 Y. Shibuta, R. Arifin, K. Shimamura, T. Oguri, F. Shimojo, S. Yamaguchi, *Chem. Phys. Lett.* 2013, **565**, 92-97.
- 32 W. Somers, A. Bogaerts, A. C. T. van Duin, S. Huygh, K. M. Bal, E. C. Neyts, *Cat. Today* 2013, **211**, 131-136.
- 33 B. Liu, M. T. Lusk, J. F. Ely, *Surf. Sci.* 2012, **606**, 615-623.
- 34 C. P. Deck, K. Vecchio, *Carbon* 2006, **44**, 267-275.
- 35 M. J. Mees, G. Pourtois, E. C. Neyts, B. J. Thijsse, A. Stesmans, *Phys. Rev. B* 2012, **85**, 134301.
- 36 E. C. Neyts, Y. Shibuta, A. C. T. van Duin, A. Bogaerts, *ACS Nano* 2010, **11**, 6665-6672.
- 37 A. C. T. van Duin, S. Dasgupta, F. Lorant, W. A. Goddard III, *J. Phys. Chem. A* 2001, **105**, 9396-9409.
- 38 J. E. Mueller, A. C. T. van Duin, W. A. Goddard III, *J. Phys. Chem. C* 2010, **114**, 4939-4949.
- 39 G. Bussi, D. Donadio, M. Parrinello, *J. Chem. Phys.* 2007, **126**, 014101.
- 40 S. Maruyama, T. Kurashige, S. Matsumoto, Y. Yamaguchi, T. Kimura, *Micro Thermophys. Eng.* 1998, **2**, 49-62.
- 41 T. R. Cundari, S. S. Janardan, O. Olatunji-Ojo, B. R. Wilson, *Inter. J. Quant. Chem.* 2011, **111**, 4303-4308.

- 42 M. Moors, H. Amara, T. V. de Bocarmé, C. Bichara, F. Ducastelle, N. Kruse, J.-C. Charlier, *ACS Nano* 2010, **3**, 511-516.
- 43 G. Henkelman, B. P. Uberuaga, H. Jonsson, *J. Chem. Phys.* 2000, **113**, 9901.
- 44 J. E. Mueller, A. C. T. van Duin, W. A. Goddard III, *J. Phys. Chem. C* 2010, **114**, 5675-5685.
- 45 M. Zhu, J. Wang, B. C. Holloway, R. A. Outlaw, X. Zhao, K. Hou, V. Shutthanandan, D. Manos, *Carbon* 2007, **45**, 2229-2234.
- 46 F. Ohashi, G. Y. Chen, V. Stolojan, S. R. P. Silva, *Nanotechnology* 2008, **19**, 445605
- 47 G. Zhang, P. Qi, X. Wang, Y. Lu, X. Li, R. Tu, S. Bangsaruntip, D. Mann, L. Zhang, H. Dai, *H. Science* 2006, **314**, 974-977.
- 48 G. Zhang, P. Qi, X. Wang, Y. Lu, D. Mann, X. Lu, H. Dai, *J. Am. Chem. Soc.* 2006, **128**, 6026-6027.
- 49 M. J. Behr, E. A. Gaulding, K. A. Mkhoyan, E. S. Aydil, *J. Vac. Sci. Technol. B* 2010, **28**, 1187-1194.
- 50 C. T. Brooks, S. Peacock, B. G. Reuben, *J. Chem. Soc., Faraday Trans.* 1979, **75**, 652-662.
- 51 M. H. Back, *Canadian Journal of Chemistry* 1971, **49**, 2199-2204.
- 52 K. M. Ervin, S. Groner, S. E. Barlow, M. K. Gilles, A. G. Harrison, V. M. Bierbaum, C. H. DePuy, W. C. Lineberger, G. B. Ellison, *J. Am. Chem. Soc.* 1990, **112**, 5750-5759.
- 53 F. Stahl, P. v. R. Schleyer, H. F. Schaefer III, R. I. Kaiser, *Planetary and Space Science* 2002, **50**, 685-692.
- 54 M. B. Colket, *Preprints of the Division of Fuel Chemistry, Am. Chem. Soc.* 1986, **31**, 98-107.
- 55 R.S. Slysh, C.R. Kinney, *J. Phys. Chem.* 1965, **65**, 1044-1045.
- 56 W. Eisfeld, *Phys. Chem. Chem. Phys.* 2005, **7**, 3924-3932.
- 57 F. Cataldo, *Ultrason. Sonochem.* 2000, **7**, 35-43.
- 58 T. Tanzawa, Jr. W. C. Gardiner, *J. Phys. Chem.* 1980, **84**, 236-239.
- 59 A. Malesevic, S. Vizireanu, R. Kemps, A. Vanhulsel, C. Van Haesendonck, G. Dinescu, *Carbon* 2007, **45**, 2932-2937.